SAR Wind Measurements for Wind Climatology: Application to Wind Power

Lecture

Remote Sensing for Wind Energy
Boulder, Colorado, June 11-15, 2012

Frank Monaldo
Johns Hopkins University Applied Physics Laboratory
11100 Johns Hopkins Road, Laurel MD 20723
frank.monaldo@jhuapl.edu

1 Introduction

The siting of power plants offshore poses challenges different from the placement of similar facilities on shore, and the costs of offshore installations makes sub-optimal deployments more expensive. In addition, offshore measurements of wind field statistics are generally rarer and of less spatial densities. Remote sensing of wind field climatologies offers the opportunity to assess offshore wind fields relatively inexpensively. The sub-kilometer resolution wind fields measured by spaceborne synthetic aperture radars (SARs) have recently be applied to problem. This application is the focus of this short paper

Here we will provide a description of:

- SAR measurement of normalized radar cross section at high-resolution.
- The relationship between SAR-measured normalized radar cross section and wind speed.
- An operational software package that routinely converts SAR-measured radar cross into wind speed.
- Application of SAR wind speed measurements to wind climatologies.

2 High-resolution Radar Images

2.1 The Basics

Synthetic aperture radars from space typically have ground resolutions of 25 m and as fine as 3 m. To first order, and ignoring details about the antenna, then angular beam-width of an antenna is given by

$$\beta = \lambda / D \tag{1}$$

where λ is the radar wavelength and D is the width of the antenna. Assume we have satellite in polar orbit, with a typical off-nadir slant range of 830 km, then the angular field of view required to achieve 25 m resolution would be about 3×10^{-5} radians. Spacborne SAR wavelengths range from over 20 cm to about 3 cm, with 5 cm being the most common. Using Equation 1, an antenna would have to be over 1500 m. Of course, this size of a physical antenna is impractical. This is why SARs create a very long "synthetic" antenna through signal processing. How a SAR achieves high resolution is illustrated in Figure 1.

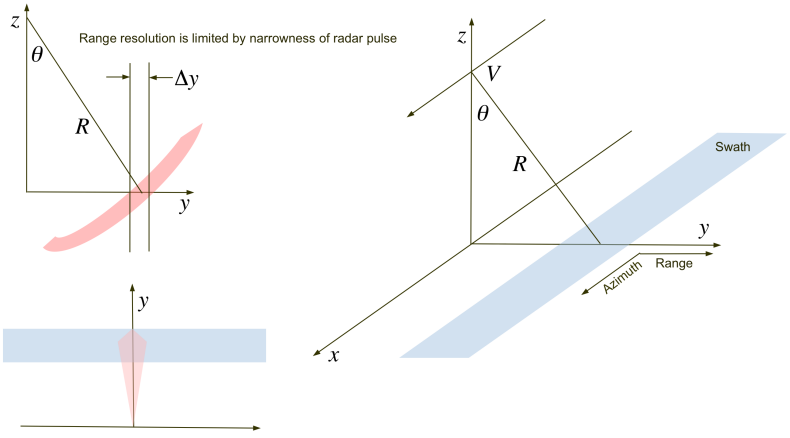

Figure 1: SAR geometry.

Table 1: Summmary of spaceborne SARs. For some of the later SARs with many modes, we limited the table entries. Resolution values also vary depending on the number of looks. Full-polarization SARs can also operate in more limited polarization modes to increase swath width. The purpose of this table is to provide perspective on the improvement of spaceborne SAR systems. Frequency band definitions. L-band: 1–2 GHz, 10–30 cm; C-band: 4–8 GHz, 3.75–7.5 cm; X-band: 8-12 GHz, 2.4–3.75 cm.

Satellite	Launch	Frequency	Polarization	Resolution
Seasat	1978	L	HH	25 m
SIR-B	1984	L	HH	16–58 m
ERS-1	1991	C	VV	25 m
JERS-1	1992	L	HH	18 m
SIR-C	1994	L	Full-pol	10–50 m
		C	Full-pol	10–50 m
		X	VV	10–50 m
ERS-2	1995	C	VV	25 m
Radarsat-1	1995	C	HH	25–50 m
SRTM	2000	C	HH,HV,VH,VV	30 m
		X	VV	30 m
Envisat	2002	C	VV, HH, VV/HH, HV/HH, VH/VV	30–1000 m
ALOS	2006	L	Full-pol	7–88 m
TerraSAR-X	2007	X	Full-pol	3 m
Radarsat-2	2007	C	Full-pol	3–100 m
COSMO-SkyMed	2007	X	Full-pol	3 m

SARs generally create an image swath off-nadir to the SAR platform flight path. Distance along the flight track in this swath is identified as the azimuth direction. The range direction is perpendicular to the flight path.

In the range direction, high resolution can be achieved by transmitting a narrow radar pulse. Range resolution is thus not limited by the antenna, but by how narrow this pulse can effectively be made. However, in the azimuth direction, resolution is still limited by the size of the antenna.

A large synthetic aperture is created by examining the Doppler shift of the return radar pulse. When an object on the ground enters the wide real aperture antenna beam, the relative velocity between the SAR platform the object is V, with the associated Doppler shift in frequency. As the SAR flies along at some point the object will be perpendicular to the SAR flight direction and the relative velocity is zero. Later the relative velocity approaches $-V$. We can locate the azimuth position of the object at the point of zero Doppler shift. Hence, azimuth resolution is not limited not be antenna size, but by the precision with which one can measure Doppler shifts.

3 History

The first civilian SAR in space was Seasat, launched in 1976. Since then a number of SAR satellites have been launched. These are listed in Table 1. Over time the technology has improved, with satellites launched at a variety of radar frequencies. While early SARs operated at a single polarization, new SARs include the option of operating at a variety of transmit/receive polarizations. Full-polarization SARs, permit the reconstruction of any transmit/receive polarization pair.

Figure 2 is a illustration of the quality of modern SARs. This image shows the Straights of Gilbraltar as acquired by TerraSAR-X. This resolution permits the imaging of variations of cross section associated

with not only wind, but also ships and their wakes.

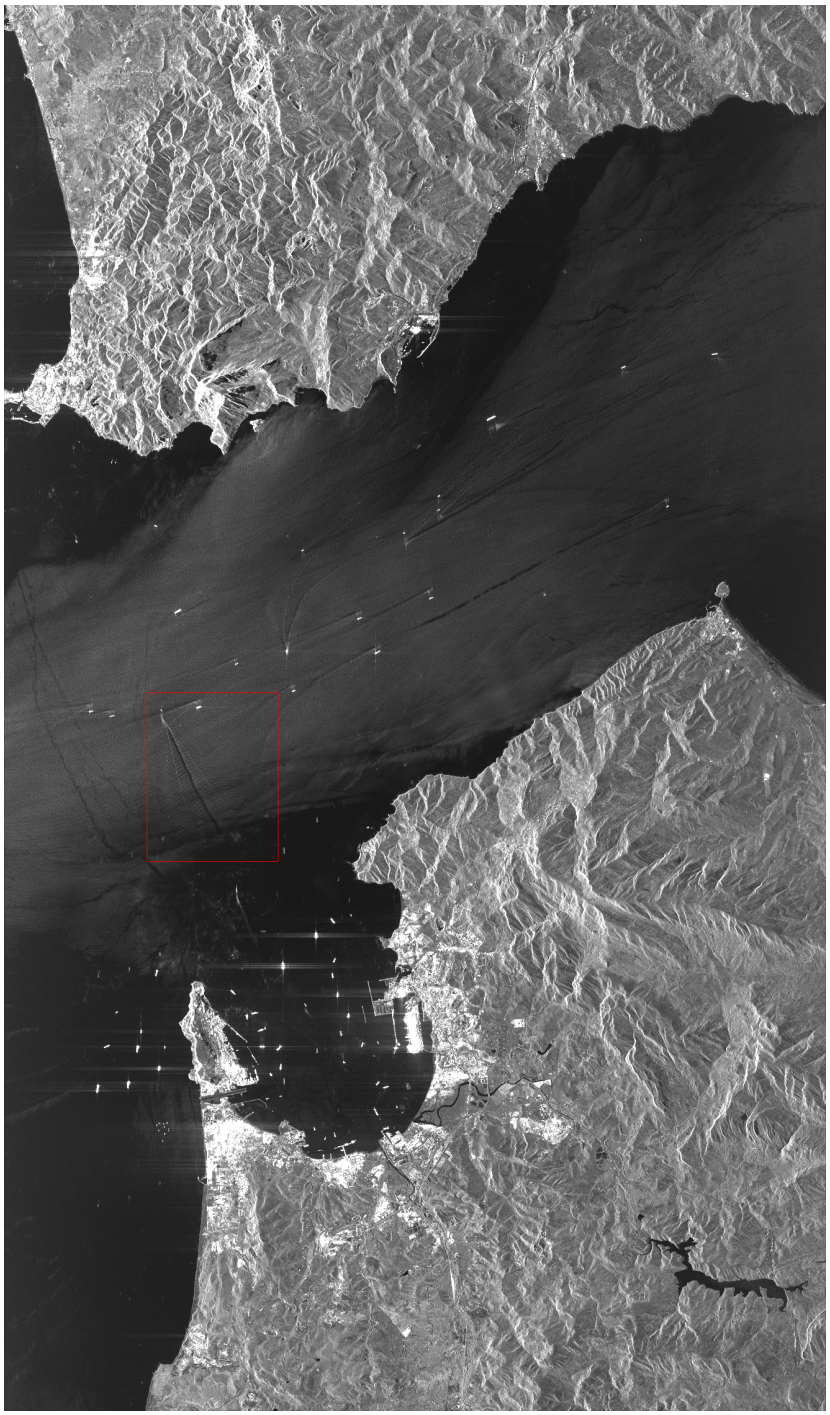

Figure 2: Sample high-resolution NRCS image from TerraSAR-X. The outlined illustrates the imaging of ship wakes.

4 Wind Speed and the Ocean Surface

Backscattered microwave radar returns from the ocean surface are strongly dependent on wind speed and direction. The physics underlying the measurement of marine wind speed by radar can be observed by a casual walk along a pond or lake. When no wind is present, the surface of the water is smooth, almost glass-like. As the wind begins to blow, the surface roughens and surface waves begin to develop. As the wind continues to blow more strongly, the amplitude of the waves increases, roughening the surface still more. Careful examination of the wind-generated waves reveals that these surface wave crests are generally aligned perpendicular to the prevailing wind direction.

The backscattering of microwave radar power from a wind-roughened surface — i.e., the normalized radar cross section (NRCS) — is critically dependent on the surface roughness and its structure. At moderate incident angles, 20° to 60° from nadir, nearly all of the radar energy directed at a smooth water surface will reflect away from the direction of the incident beam at an angle from the local vertical equal to that of the incident beam, much like optical reflection from a mirror. This is called "specular scattering." As the surface roughens, however, more of the incident radiation will be reflected back toward the radar. The scattering process becomes significantly more complicated.

There are analytical means for modeling the effect of wind on the structure of the ocean surface and the consequent electromagnetic backscattering. This remains an important area of research [1, 2, 3, 4, 5, 6]. However, from a practical stand point, the relationship between wind speed and direction and the resulting radar cross section is generally expressed as an empirical geophysical model function (GMF) of the form:

$$\sigma^0 = u^{\gamma(\theta)} A(\theta)[1 + B(u,\theta)\cos\phi + C(u,\theta)\cos 2\phi] \tag{2}$$

where σ^0 is NRCS, u is wind speed at 10 m above the surface for neutral atmospheric stability, γ is an exponent dependent upon the radar incident angle θ, A is a coefficient also dependent upon θ [7, 8]. The coefficients B and C are dependent on wind speed and incident angle. The angle between the radar look direction and the wind direction is ϕ.

Equation 2 has some obvious properties. As wind speed increases, NRCS increases. NRCS is also strongly dependent on ϕ. When $\phi = 0$, the radar looking into the wind, the NRCS is a maximum, falling to a minimum for cross wind, $\phi = \pm\pi/2$. For $\phi = \pi$, where the radar and the wind are anti-parallel, there is another smaller maximum in NRCS.

The salient features of such model functions are illustrated in Figure 2. This plot shows C-band microwave backscatter (≈ 5 cm wavelength) using the CMOD5 GMF [8] for 40° incidence. The x-, y-, z-axes represent wind speed, the relative angle between the radar and wind directions, and radar cross section, respectively. NRCS increases with wind speed until about 35 m/s, where the NRCS drops again. For our purposes, such high wind speeds are rarely reached. It is clear that for any particular wind speed and direction there is a specific NRCS. However, the reverse is not true. For any given NRCS, there may be many different combinations of wind speed and direction to which the NRCS value corresponds. This is the fundamental challenge in estimating the wind vector from spaceborne microwave radars.

There are several different approaches for performing wind speed retrievals from spaceborne radar measurements of backscatter. Spaceborne radar scatterometers, like those aboard QuikSCAT and ASCAT, use multiple looks from multiple antennas or a rotating antenna to measure the NRCS of the same spot on the ocean from different incident and aspect angles. This usually allows (with the aid of numerical weather model predictions) an unambiguous wind vector retrieval from Equation 2. Unfortunately, conventional spaceborne scatterometers typically have 25 km resolution and are of limited utility in coastal regions for wind resource climatology. Conventional scatterometers were designed for operation in the open ocean.

Synthetic aperture radars (SARs) create high-resolution (3–100 m) images of radar cross section. After the first SAR was launched in 1978 on Seasat. NRCS variations were quickly recognized as manifestations of wind speed variations [9, 10, 11]. Gerling [12] was able to demonstrate the ability

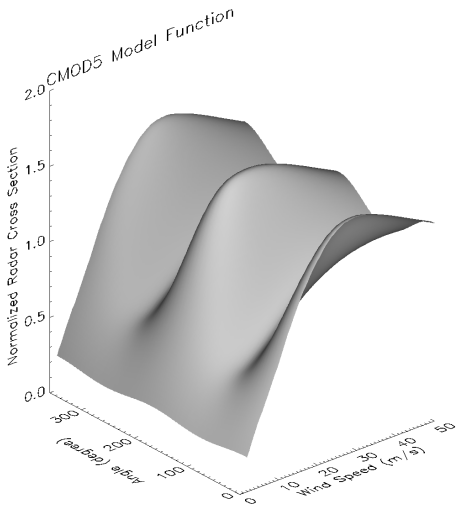

Figure 3: CMOD5 geophysical model function for 40° *incidence.*

to retrieve wind speed and direction from Seasat. Later, a number of investigators [13, 14, 15] demonstrated wind vector retrievals with ERS-1/2 satellites.

The key challenge with respect to SAR wind speed retrieval is to obtain an estimate of the wind direction. If the direction is known, Equation 2 can be directly inverted to compute wind speed. There are two basic approaches to obtaining these directions. The first is to use wind directions estimated from numerical weather forecast models. The second is to estimate the wind direction (with a 180° ambiguity) from linear features aligned with the wind [12] in the image .

The advantage of the first method is that a dynamically balanced realistic wind direction is always available, though high-resolution variations in direction might be missed. The second method may pick up the higher spatial frequency variations, but sometimes linear features are not detectable or may be associated with phenomena other than winds. A number of investigators [16, 17, 18] systematically compared Radarsat-1 wind speed retrievals (using both wind direction approaches) with model predictions, buoys and QuikSCAT data and found wind speed accuracy of better than 2 m/s. A comprehensive consensus view on SAR wind retrievals was published in the proceeding of the Second Workshop on Coastal and Marine Applications of SAR [19].

Figure 4 is a sample of wind speed retrieved from a Radarsat-1 SAR image off the Delaware Bay. The white arrows represent the SAR look direction. The blue arrows are wind direction from the Navy Operational Global Atmospheric Prediction System (NOGAPS). The pseudo colors represent retrieve wind speed using NOGAPS directions and the Radarsat-1 NRCS values to compute the wind.

Monaldo et al. [16] used ANSWRS to systematically compare Radarsat SAR wind speed retrievals against National Data Buoy Center (NDNC) buoys. Averaging SAR wind speeds over a 3 km $\times$ 3 km area and having no more than a 30 minute separation between SAR acquisition and buoy measurement, they found agreement to within 1.70 m/s. See Figure 5. Later work [17] comparing Radarsat-1 wind speed retrievals with QuikSCAT achieved similar results.

5 ANSWRS

Despite the apparent ability of SARs to make high-resolution wind measurements, until the late 1990s, these retrievals were made on a sporadic basis for research purposes. The US launched the Canadian

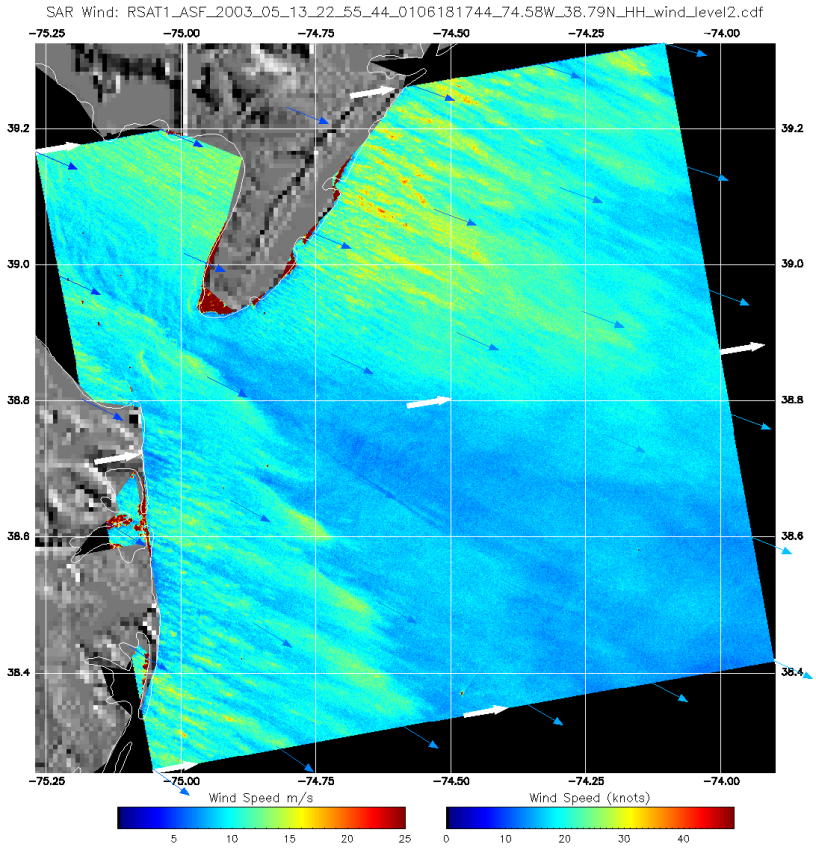

Figure 4: Radarsat-1 wind speed imaged off the Delaware Bay. The image was acquired at 2003 May 13 12:22:54 UTC. A topographic map is superimposed on the land areas. NRCS values over land are not related to wind speed.

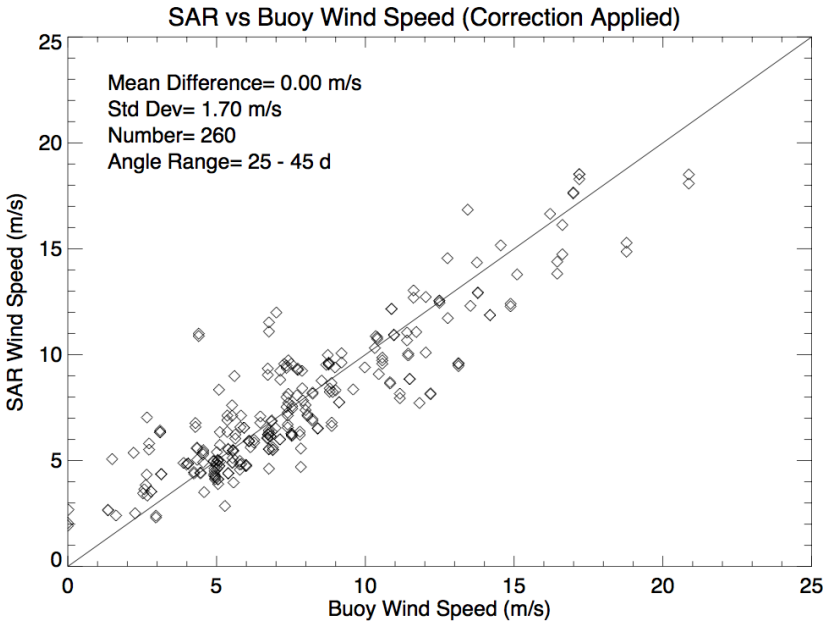

Figure 5: Radarsat-1 wind speed retrievals compared to NDBC buoy measurements.

Radarsat-1 in 1995. Since the US provided the launch, it was entitled to a significant fraction of the data acquired. The Alaska Satellite Facility[1] (ASF) downloaded and processed into imagery, data acquired while Radarsat-1 was within the ASF reception mask as well as in other areas. Given the large quantity of Radarsat-1 SAR data near Alaska and the lack of wind measurements off the enormous coast of Alaska, NOAA began the StormWatch Program [20] and asked the Johns Hopkins University Applied Physics Laboratory (JHU/APL) to help it to determine how well a SAR could be used to make coastal wind measurements [21, 22].

Over time, this work grew into ANSWRS (APL/NOAA SAR Wind Retrieval System). ANSWRS can compute wind field maps within 10 minutes of the time the SAR imagery are available. The Alaska Satellite Facility (ASF) provided Radarsat-1 to NOAA in less than two hours, allowing near-real-time wind speed maps to be posted to the web. In addition, ANSWRS can now process SAR images from ERS-1/2, Radarsat-1/2, Envisat, ALOS, TerraSAR-X, and Cosmo-SkeyMed into wind speed images.

NOAA is now taking the ANSWRS system operational. As part of this effort, JHU/APL is migrating ANSWRS to ANSWRS 2.0. The key difference is that the new system is more modular, easier to maintain, easier to incorporate new GMF's into, and easier to add data from new SARs to as they become available. In addition, intermediate data products are stored so that users will have access to the data at any point: from the NRCS data, to the wind data in the original coordinates of the image, to wind data re-sampled to a rectilinear longitude-latitude grid.

6 Sample of Maryland Wind Climatology

6.1 Data Used to Create the Maryland Offshore Wind Climatology

During the period of 1996 to 2008, when NOAA was taking advantage of its Radarsat-1 data allocation, SAR data processed at ASF and Gatineau, were archived in NOAA's Comprehensive Large Array-data Stewardship System (CLASS).[2] It is from this extensive archive that we acquired those Radarsat-1 SAR

[1] Formerly known as the Alaska SAR Facility.

[2] http://www.class.ngdc.noaa.gov/saa/products/welcome

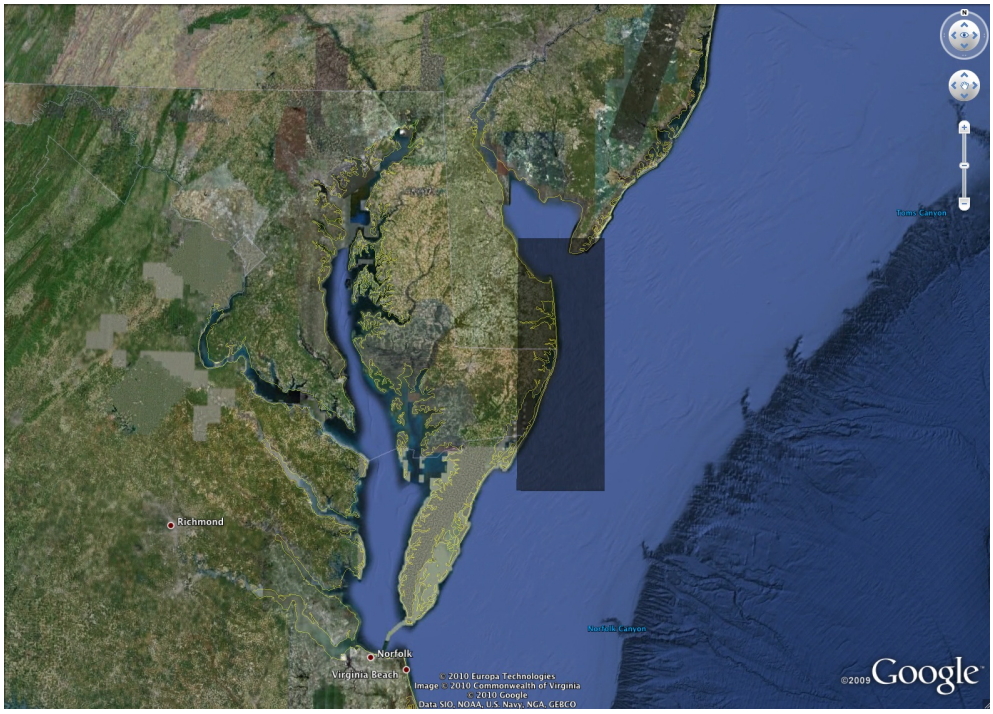

Figure 6: Maryland wind climatology study area.

images off the coast of Maryland. The designated region of interest is 75.30°W to 74.75°W in longitude and 37.75°N to 39.00°N, shown as a darkened area in Figure 6.

Table 2 lists the number of available Radarsat-1 images from CLASS by year. There were 1495 available images. A first cut through the data eliminated 44 images where NRCS values were zeroed-out due to processing failures. We processed the remaining 1451 images into wind speed images. Of these, 12 suffered from anomalies that made their inclusion in any statistical analysis inappropriate. After systematically examining all the wind images and removing the unsuitable ones, 1439 remained.

6.2 Normalization

With satellite data, there is always the possibility that we are sampling the wind field in a systematically biased way. If the seasonal distribution of images is skewed, the resulting fields might be as well. Figure 7 shows the monthly distribution of the 1439 images we used.

There is a rather flat distribution of images as a function of month, save that January is significantly over represented in comparison to other months. Hence, to compute a fairer average of the wind speed and wind power, the data from more sparse months needs to be weighted more heavily. Specifically, if $N_{\max}$ represents the number of images in the month with the maximum number, *i.e.,* January, then the weighting applied to the months, w_i, is

$$w_i = \frac{N_{\max}}{N_i} \tag{3}$$

where N_i represents the images in month i.

In presenting the following data, we have presented results with and without normalization. Since there is only one month with a significantly different number of available images, the normalization only slightly reduces mean wind and mean power fields.

Table 2: Number of available images by year.

Year	Number	Processed	Used
1996	10	9	5
1997	29	31	15
1998	126	119	118
1999	137	137	134
2000	141	140	283
2001	214	205	180
2002	223	215	195
2003	162	144	133
2004	89	89	76
2005	73	69	63
2006	145	145	126
2007	128	130	93
2008	18	18	18
Total	1495	1451	1439

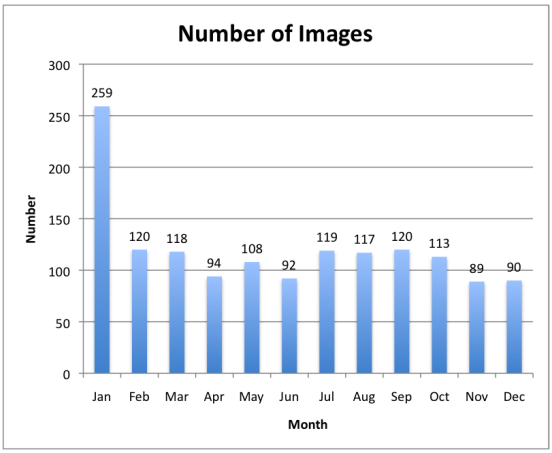

Figure 7: Monthly distribution of 1439 available images.

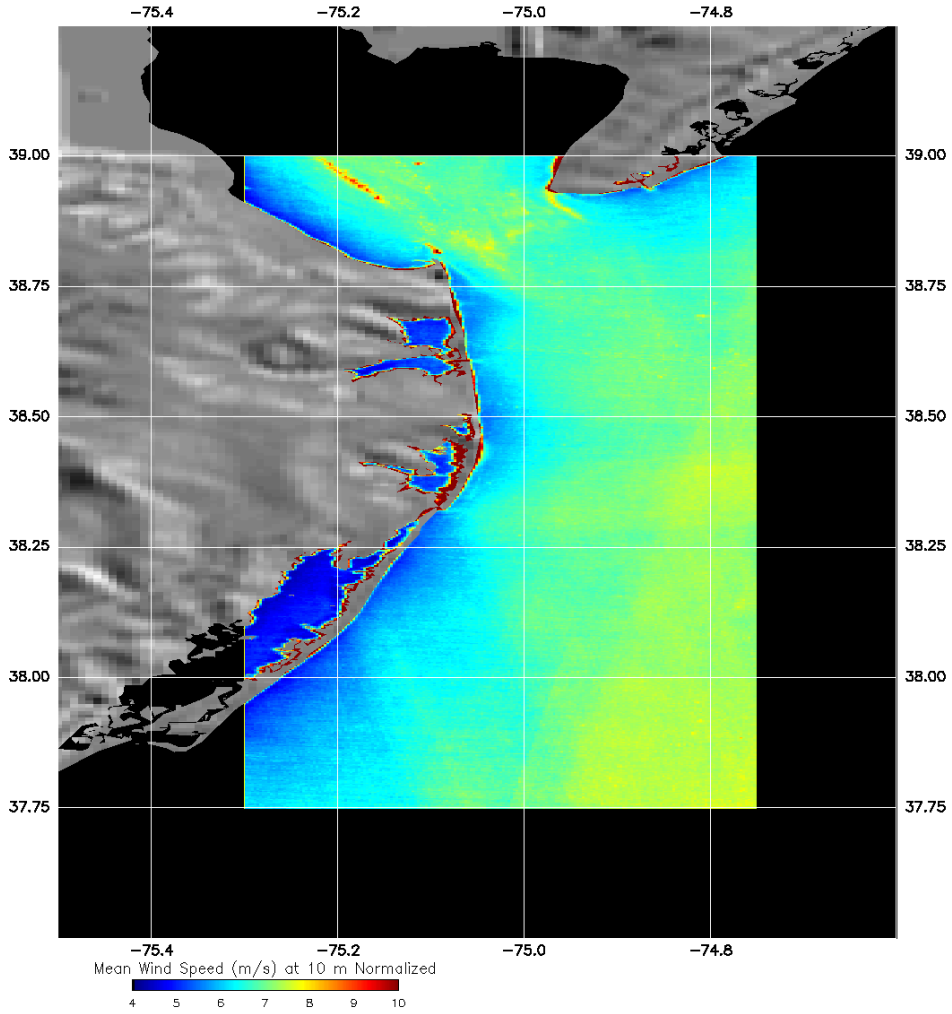

Figure 8: Radarsat-1 mean wind speed field from 1996–2008 at a 10-m height for neutral atmospheric stability. The data have been normalized so that no month is over represented.

6.3 The Wind Speed Climate

6.3.1 Mean Wind Speed Field

We constructed the mean wind field for the area under consideration using the final 1439 images. For our proposes, here we resampled this images to rectilinear longitude-latitude grid with a 250-m sampling. At each geographical pixel location the mean wind speed was computed. Figure 8 is pseudo-color representations of the mean wind speed at 10 m above the surface from the entire data set of SAR images from 1996 to 2008, normalized. Note the rather uniform wind field structure and the fact that wind speed increases at regular rate, as expected, the further the distance from shore.

With respect to the wind power application, the relevant wind speed is the wind speed at the height of the blades above the surface. Wind speed as a function of altitude is usually modeled logarithmically using a function of the form

$$u(z) = \frac{u_*}{\kappa} \ln \frac{z}{z_0} \tag{4}$$

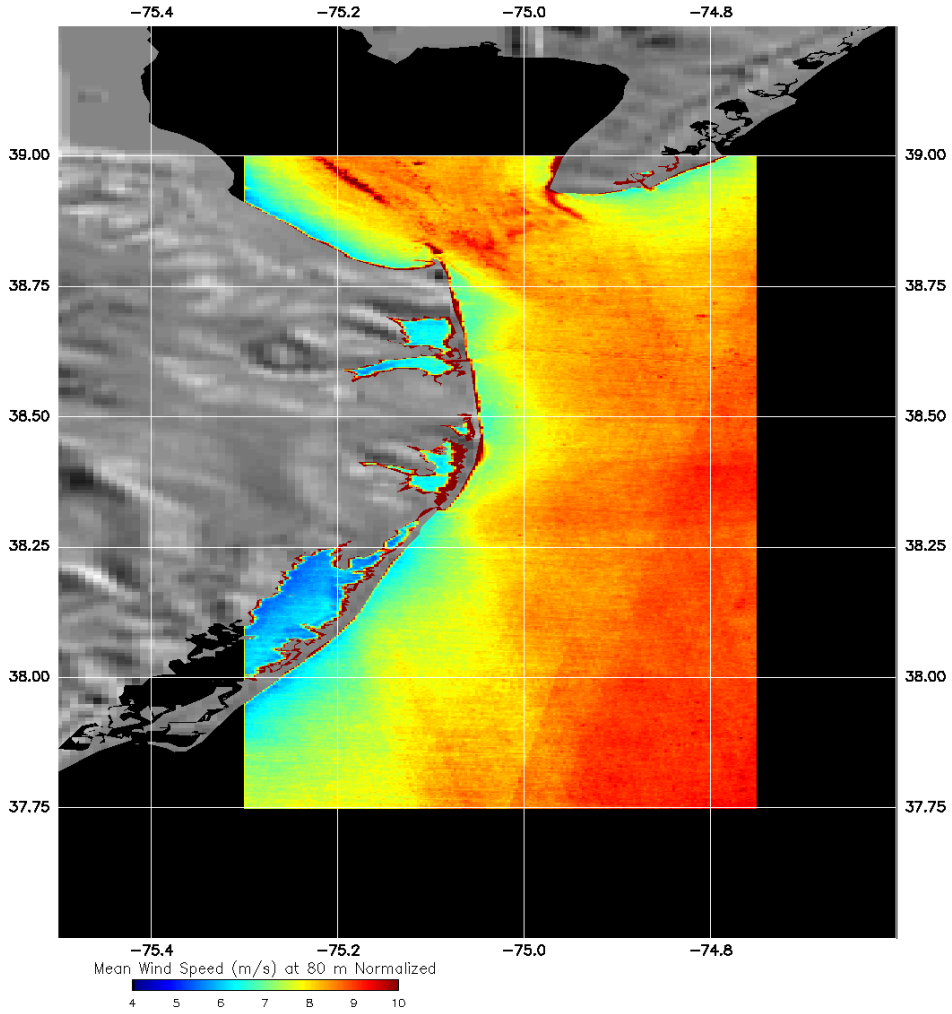

Figure 9: Radarsat-1 mean wind speed field from 1996–2008 at a 80-m height for neutral atmospheric stability. The data have been normalized so that no month is over represented.

where u is wind speed u_* is friction velocity κ is von Karmon constant (0.4), z is altitude, and z_0 is roughness length. For coastal open ocean, z_0 is about 0.001 m [23]. Assuming 80-m height for a wind turbine hub, we solve for the wind speed at 80 m as a function of the wind at 10 m and yield

$$u(80) = u(10)\frac{\ln(80/0.001)}{\ln(10/0.001)} \tag{5}$$

or

$$u(80) = 1.23u(10) \tag{6}$$

Figure 9 represent the mean wind speed at an altitude of 80 m, normalized by month. The spatial structure of the wind field is unchanged, but the value of the wind speed has been significantly increased.

The energy that can extracted from the wind is dependent upon many things including the wind turbine efficiency and the area swept out blades. However, the available energy flux, Watts/m^2, is easily

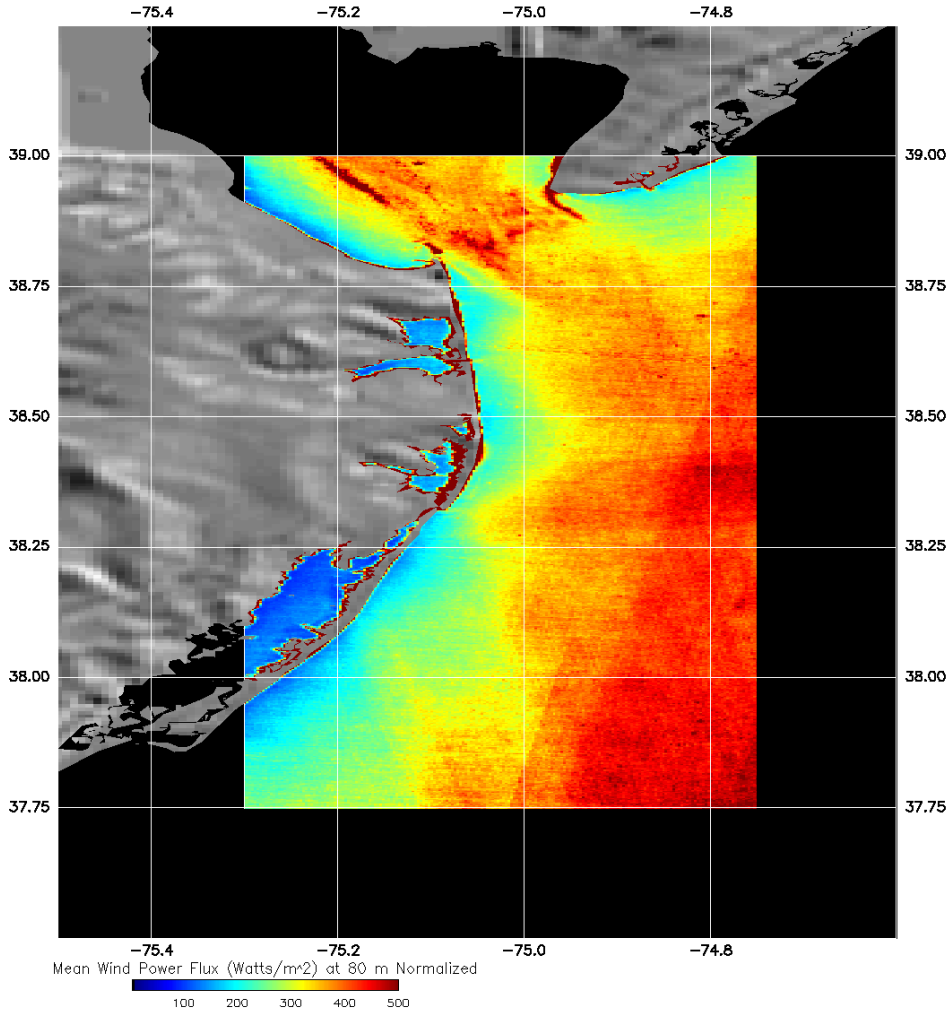

Figure 10: Radarsat-1 wind power density field computed from the mean wind field from 1996–2008 at a 80-m height. The data have been normalized so that no month is over represented.

computed as

$$P = \rho u^3/2 \tag{7}$$

where P is the power flux (power per unit area), ρ is the density of air, and u is the wind speed.[3] Using Equation 7, Figure 10 shows the resulting power density map for a 80-m hub height and a neutrally stable atmosphere, both un-normalized and normalized.

6.3.2 Variation With Distance From Shore

Although pseudo-color images of wind speed and power are a powerful indicator of the spatial variability of the mean wind and power fields, the variations with respect to distance from shore more directly address questions about wind turbine placement. Figures 11, 12, 13, 14, and 15, represent the wind speed variation at 10-m and 80-m heights, both un-normalize and normalized, as a function of distance

[3] American Wind Energy Association. *http://www.awea.org/faq/windpower.html*

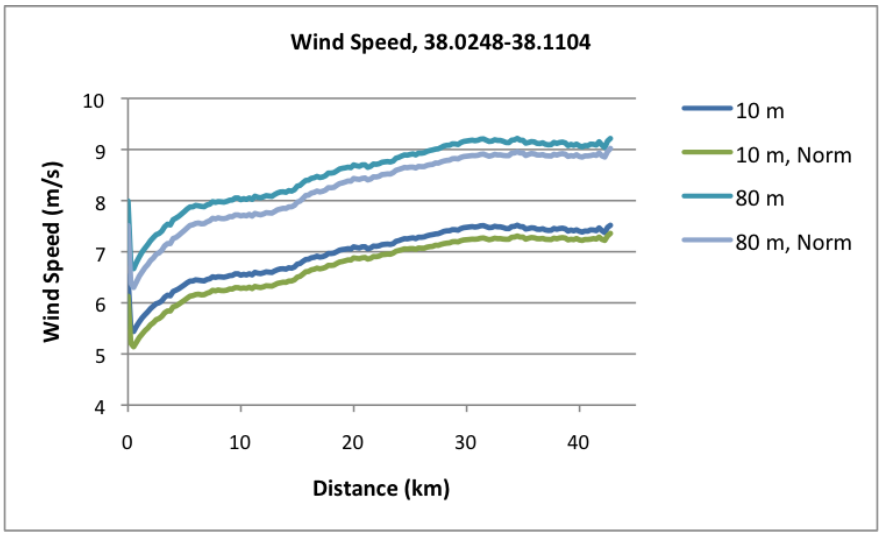

Figure 11: Radarsat-1 mean wind speed from 1996–2008 at a 10-m and 80-m heights, un-normalized and normalized as function of distance from shore in the latitude range 38.0248°*N to* 38.1104°*N.*

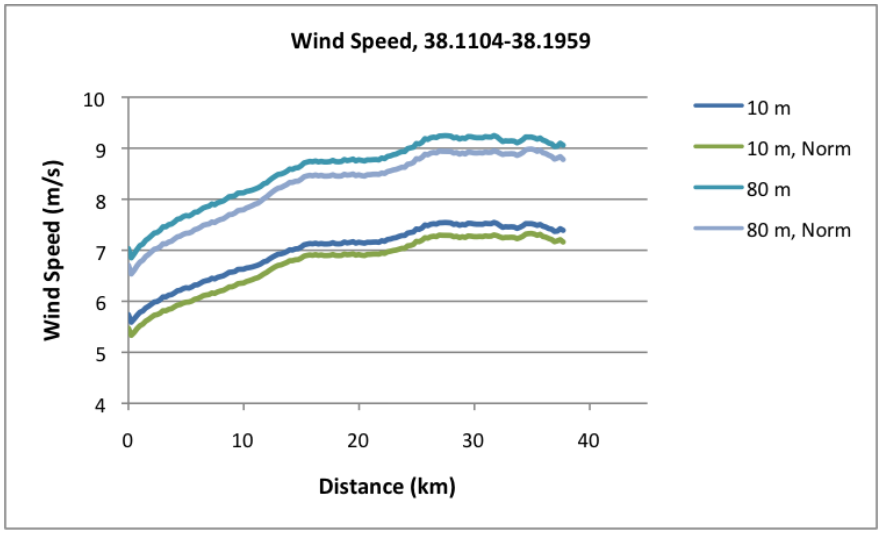

Figure 12: Radarsat-1 mean wind speed from 1996–2008 at a 10-m and 80-m heights, un-normalized and normalized as function of distance from shore in the latitude range 38.1104°*N to* 38.1959°*N.*

from shore for the latitude bands spanning the Maryland coast, 38.0248°N to 38.1104°N, 38.1104°N to 38.1959°N, 38.1959°N to 38.2815°N, 38.2815°N to 38.3671°N, and 38.3671°N to 38.4550°N, respectively.

Note that the variation of wind speed from shore is fairly gradual from about 6 to 8 m/s. Near zero distance from shore there appears to be sharp increase in speed. This is a consequence of land returns with high radar cross sections bleeding into the wind speed retrievals from a 1-km width running average used to smooth the data.

This gradual increase in wind speed with distance from shore maps into a more dramatic increase in wind power from shore. This is a consequence of the fact that potential wind power flux is proportional

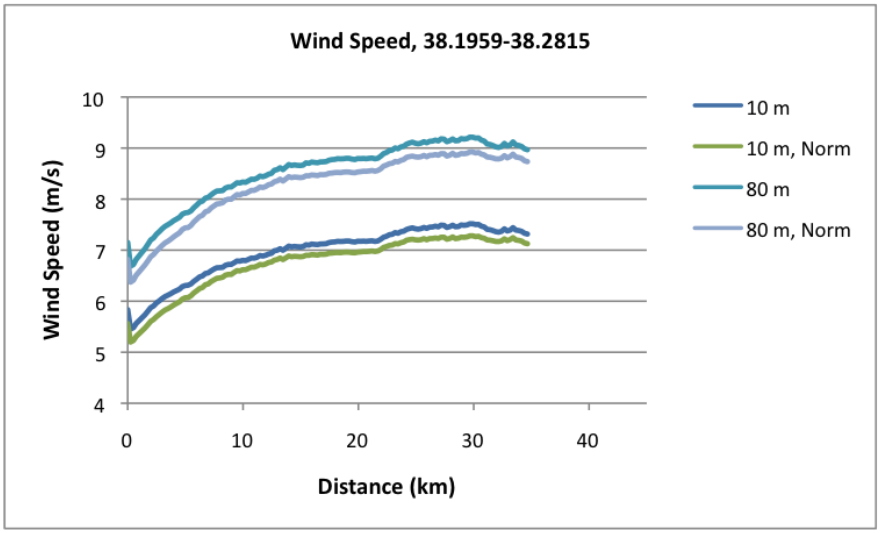

Figure 13: Radarsat-1 mean wind speed from 1996–2008 at a 10-m and 80-m heights, un-normalized and normalized as function of distance from shore in the latitude range 38.1959°*N to* 38.2815°*N.*

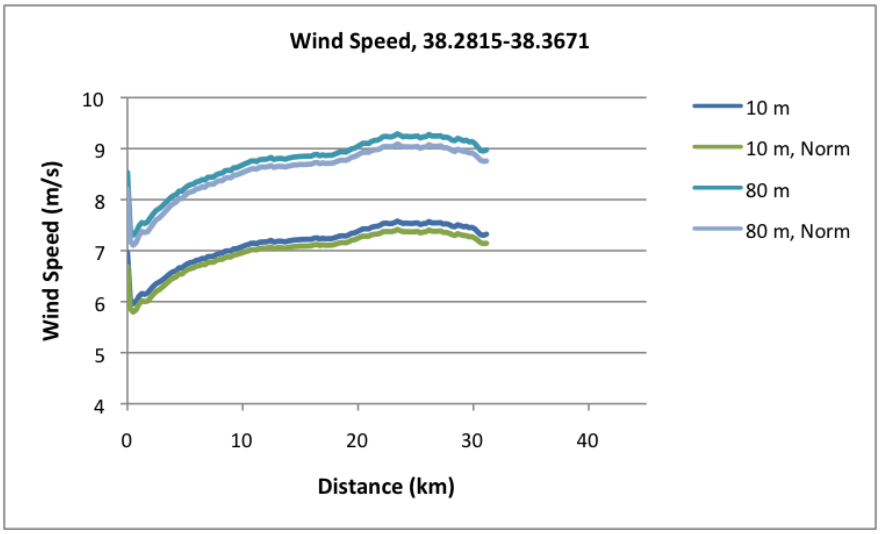

Figure 14: Radarsat-1 mean wind speed from 1996–2008 at a 10-m and 80-m heights, un-normalized and normalized as function of distance from shore in the latitude range 38.2815°*N to* 38.3671°*N.*

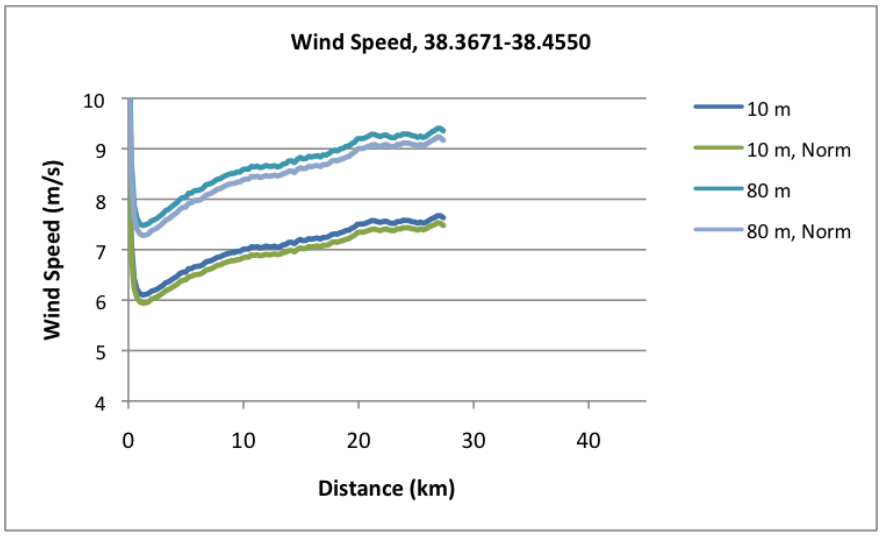

Figure 15: Radarsat-1 mean wind speed from 1996–2008 at a 10-m height as function of distance from shore in the latitude range 38.3671°*N to* 38.4550°*N.*

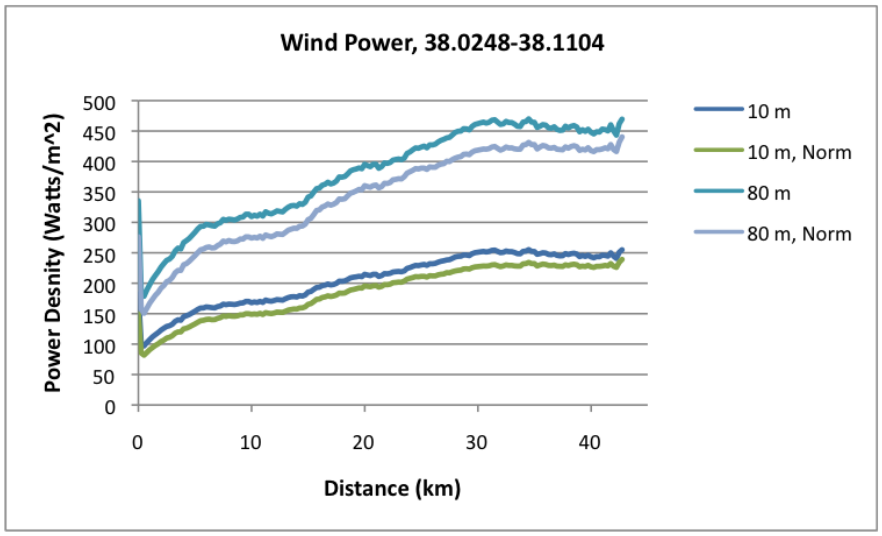

Figure 16: Radarsat-1 mean wind power from 1996–2008 at a 10-m and 80-m heights, un-normalized and normalized as function of distance from shore in the latitude range 38.0248°*N to* 38.1104°*N.*

to the cube of wind speed. Figures 16, 17, 18, 19, and 20, represent the wind speed variation at 10-m and 80-m heights, both un-normalize and normalized, as a function of distance from shore for the latitude bands spanning the Maryland coast, 38.0248°N to 38.1104°N, 38.1104°N to 38.1959°N, 38.1959°N to 38.2815°N, 38.2815°N to 38.3671°N, and 38.3671°N to 38.4550°N, respectively.

6.3.3 Higher Order Moments

The cubic relationship between wind speed and wind power means that wind speeds above the mean wind speed contribute more to wind power than wind speeds lower than the mean reduce the output

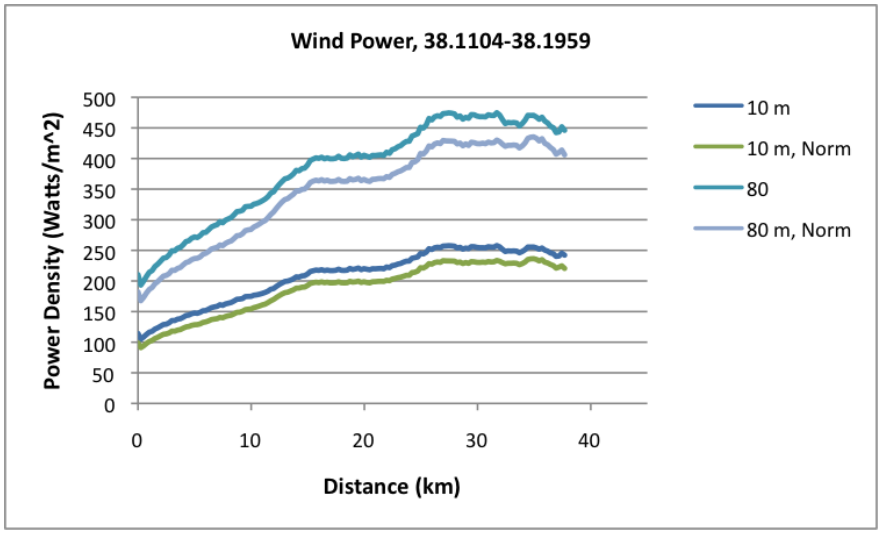

Figure 17: Radarsat-1 mean wind power from 1996–2008 at a 10-m and 80-m heights, un-normalized and normalized as function of distance from shore in the latitude range 38.1104°*N to* 38.1959°*N.*

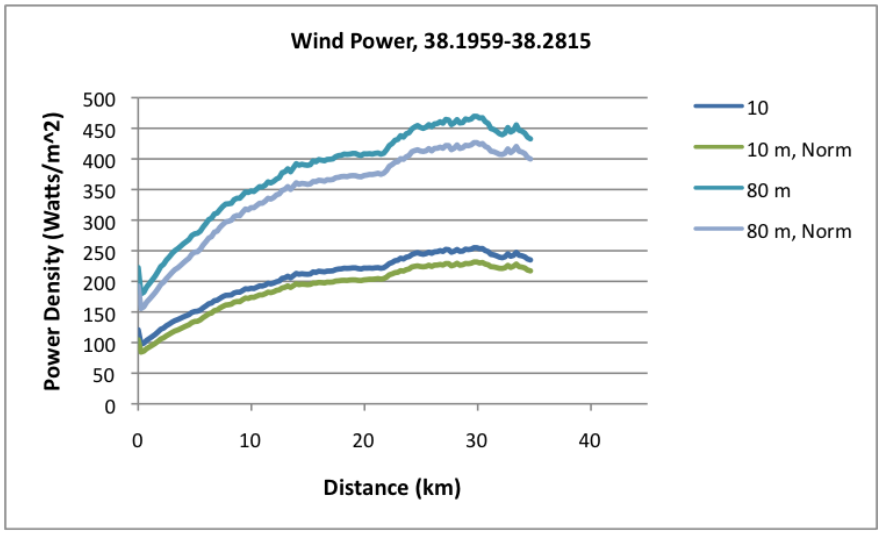

Figure 18: Radarsat-1 mean wind power from 1996–2008 at a 10-m and 80-m heights, un-normalized and normalized as function of distance from shore in the latitude range 38.1959°*N to* 38.2815°*N.*

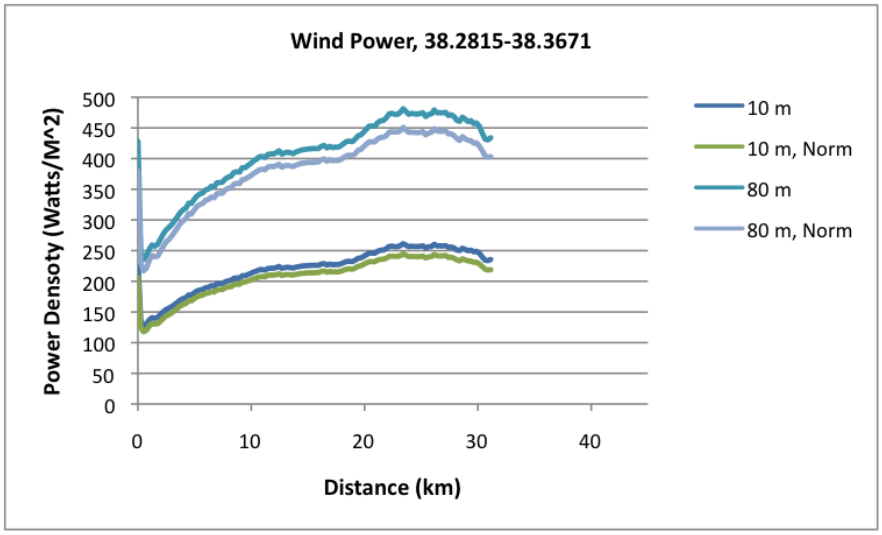

Figure 19: Radarsat-1 mean wind power from 1996–2008 at a 10-m and 80-m heights, un-normalized and normalized as function of distance from shore in the latitude range 38.2815°*N to* 38.3671°*N.*

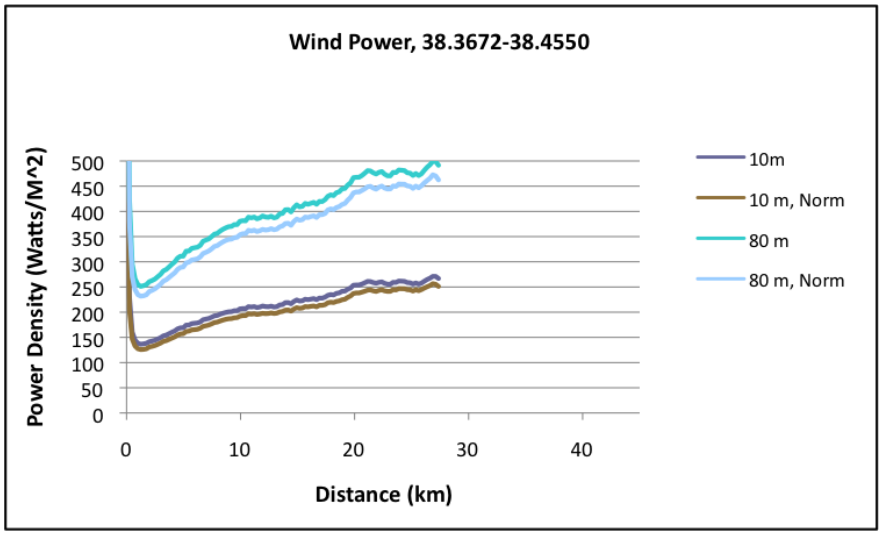

Figure 20: Radarsat-1 mean wind power from 1996–2008 at a 10-m height as function of distance from shore in the latitude range 38.3671°*N to* 38.4550°*N.*

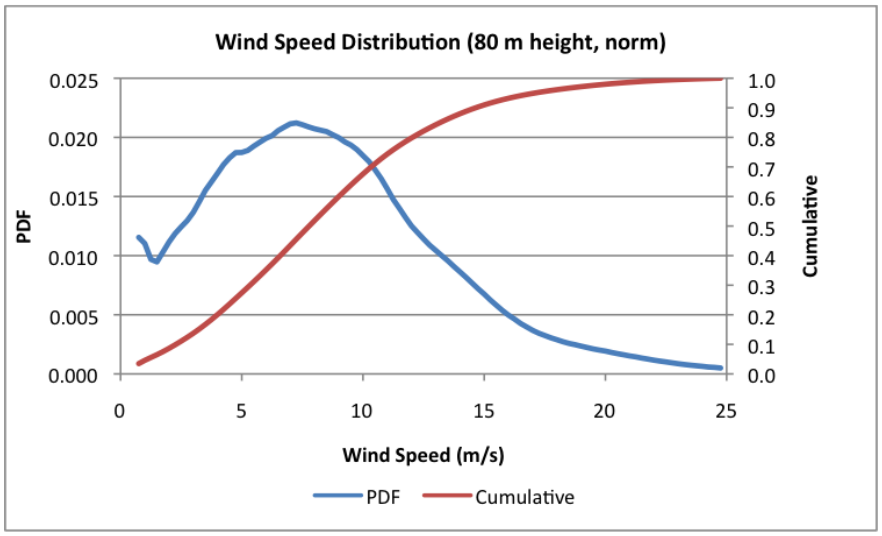

Figure 21: Wind speed distribution for all the data projected to 80-m hub height and normalized so that no month is over represented. The units of the PDF is the fractional number of wind speed measurements per 0.25 m/s bin. The computed mean wind speed is 8.36 m/s with a standard deviation of 4.79 m/s.

power. As a consequence the computed wind power flux from the wind mean underestimates the real power output. However, before we can use these higher order moments from the SAR data, their use must be validated. Mean wind speeds have been compared to buoy data and other data. However, there has been no systematic evaluation of the higher order moments of the wind speed distribution compared to wind speed distributions from buoys and other independent measurements.

In using the average wind speed field we have suppressed the effect of noise, both due to image speckle and errors in wind speed retrieval. If we have computed wind power flux for each point and then computed the power flux, any noise would have been magnified by the power law dependence. Nonetheless, the wind power flux presented here represents a conservative estimate.

6.3.4 PDF's and the Low Wind Threshold

As we have just commented, there has not been a lot of study of the accuracy of the higher order moments of wind speed as measured by SARs. In the previous subsection, we indicated a relunctance to make too much of the width of the wind speed distribution when estimating the wind power flux because the power goes as the cube of the wind speed. There needs to be a more thorough investigation as to the effect of noise and errors in the wind speed standard deviation and its impact on the wind power estimate. However, if we just consider wind speed and not wind power directly, we may be able to draw conclusions about how often we can expect wind speeds to fall with the useful range for wind power generation.

Figure 21 is wind speed probability density function (PDF) for the entire multi-year period over the entire study region. The graph is for wind speeds projected up to an 80 m/s wind turbine hub height and normalized so that no month is over represented. Note that there is a slight blip in the distribution near 0.25 m/s. This is a consequence of the fact that very low wind speeds are truncated at the low end in the wind retrieval algorithm. Nonetheless, the fraction of instances when the when speed is above or below 0.25 m/s should not be appreciably affected. The computed mean wind speed is 8.36 m/s with a standard deviation of 4.79 m/s. This corresponds to a wind power flux of about 350 Watts/m^2.

Figure 21 also shows the cumulative wind speed distribution. If we assume that wind turbines can

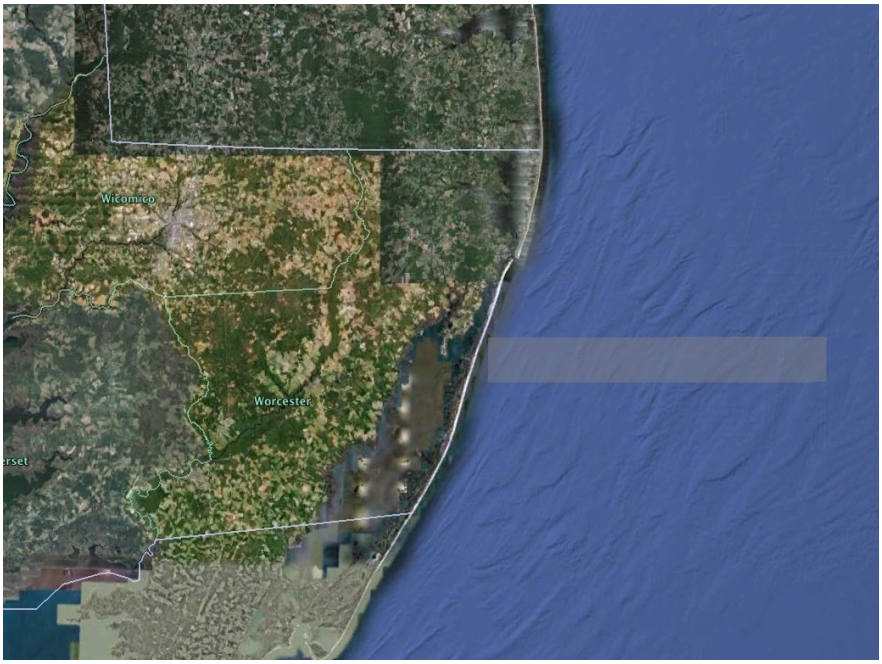

Figure 22: Area, shown in light gray, used to assess the change in threshold wind probability as a function of distance from shore.

operate in the wind speed range of 4 to 25 m/s, then approximately 80% of the time, wind turbines in this region could be operating.

The wind speed climatology images and graphs clearly show an increase in wind speed as one moves further from shore. It is, therefore, reasonable to expect that the fraction of time that wind speeds exceed 4 m/s might also increase with distance from shore. We chose to test this hypothesis starting at 75.1370°W, 38.2332°N near Assateague State Park.

The region considered is shown in Figure 22 as a shaded gray area. We divided the region into 20 partially overlapping areas approximately 0.054° by 0.054° in longitude and latitude, respectively. Within each region we computed the probability density function for 80-m hub height and normalized so that no month is over represented. Each PDF was computed from between 94,548 to 109,485 wind speed values depending on the exact region. The size of the areas is the same, but the number of available measurements in each area was not. Figure 23 represents the fraction of the time that wind speeds were observed to be greater than 4 m/s. Although there is a slight increase in the fraction of time wind speed is over a 4 m/s as function of distance from shore, the change is modest. It is clear, that for anywhere in the region, about 80% of the time wind speed is within the operational range of wing speed turbines.

As we noted in the previous section, any noise in the SAR NRCS measurements will map into a wider wind speed distribution. A narrower wind speed distribution than we observed here would increase the fraction of the time that wind speeds fall into the wind turbine operational range. Hence, the 80% value represents a conservative estimate.

7 Closing Comments

The advent of high-resolution spaceborne synthetic aperture radar wind speed measurements offers the yet to be realized potential for the optimal siting of offshore wind power plants. SARs have a

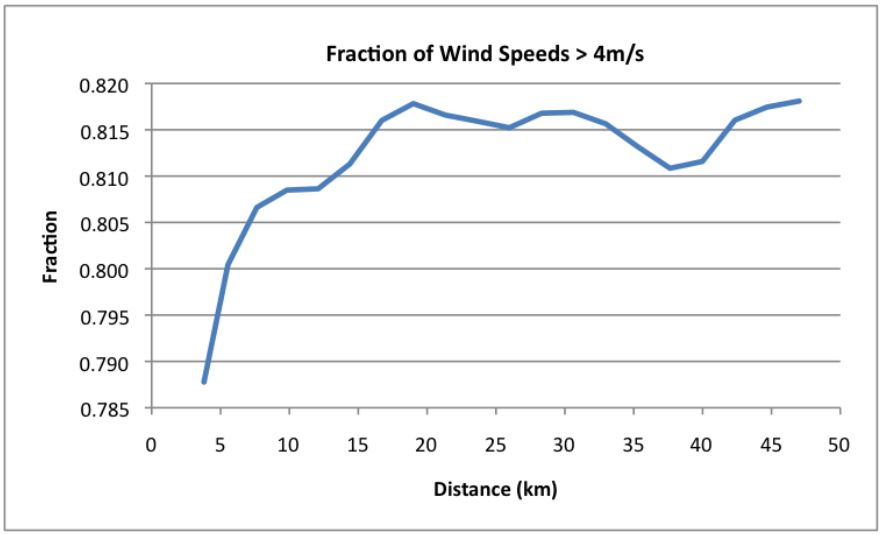

Figure 23: The fraction of wind speeds, at 80-m hub height and normalized such that no month is over represented, greater than 4 m/s as a function of distance from shore.

validated ability to measure wind speed at a sub-kilometer resolution to better than 2 m/s. The primary limitation of SARs is that they sample sporadically, and generally at the same time of day. Hence, climatologies might be biased. The best of use of SAR wind speed measurements is to validate high-resolution numerical weather model predictions of wind speed. Once such models can duplicate the measurements and spatial structure of the wind field observed from SARs, we could then compute a high-resolution climatology with greater confidence.

References

[1] P. Beckmann and A. Spizzichino, *The scattering of electromagnetic waves from rough surfaces*, New York: Macmillan, 1963.

[2] F. T. Ulaby, R. K. Moore, and A. K. Fung, *Microwave Remote Sensing: Active and Passive - Volume II: Radar remote sensing and surface scattering and emission theory*, Addison-Wesley Publishing Company, 1982.

[3] A. G. Voronovich, *Wave scattering from rough surfaces*, Springer-Verlag, Tiergartenstrasse 17, D-69121 Heidelberg, Germany, second updated edition, 1994, 236 pages.

[4] A. K. Fung, *Microwave scattering and emission model and their applications*, Artech House, 685 Canton Street, Norwood, MA, 1994, 573 pages.

[5] T. Elfouhaily, D. R. Thompson, D. Vandemark, and B. Chapron, "A new bistatic model for electromagnetic scattering from perfectly conducting random surfaces," *Waves in Random Media*, vol. 9, pp. 281–294, 1999.

[6] T. M. Elfouhaily, S. Guignard, and D. R. Thompson, "A practical second-order electromagnetic model in the quasi-specular regime based on the curvature of a 'good-conducting' scattering surface," *Waves in Random Media*, vol. 13, pp. L1–L6, 2003.

[7] A. C. M. Stoffelen and D. L. T. Anderson, "ERS-1 scatterometer data characteristics and validation of the transfer function: CMOD4," *J. Geophys. Res.*, vol. 102, pp. 5767–5780, 1997.

[8] H. Hersbach, "CMOD5 an improved geophysical model function for ERS C-band scatterometry," Internal report, European Centre for Medium-Range Weather Forecast, 2003.

[9] R. C. Beal, "The seasat sar wind and ocean wave monitoring capabilities: A case study for pass 1339m," Tech. Rep. S1R 79U–019, Johns Hopkins APL, Sept. 1980.

[10] J. F. Vesecky and R. H. Stewart, "The observation of ocean surface phenomena using imagery from the SEASAT synthetic aperture radar," *J. Geophys. Res.*, vol. 87, no. C5, pp. 3397–3430, Apr. 1982.

[11] L.-L. Fu and B. Holt, "Seasat views oceans and seas with synthetic aperture radar," Tech. Rep. JPL Publ. 81–102, Jet Propulsion Laboratory, California Institute of Technology, Pasadena, CA, 1982.

[12] T. W. Gerling, "Structure of the surface wind field from the Seasat SAR," *J. Geophys. Res.*, vol. 91, no. C2, pp. 2308–2320, 1986.

[13] F. Fetterer, D. Gineris, and C. C. Wackerman, "Validating a scatterometer wind algorithm for ERS-1 SAR," *IEEE Trans. Geosci. and Remote Sensing*, vol. 36, no. 1, pp. 479–492, 1998.

[14] C. C. Wackerman, R. Rufenach, J. Johannessen, and K. Davison, "Wind vector retrieval using ERS-1 synthetic aperture radar imagery," *IEEE Trans. Geosci. and Remote Sensing*, vol. 34, pp. 1343–1352, 1996.

[15] J. Horstmann, "Investigation of wind speed retrieval with synthetic aperture radar aboard the ERS-1/2 satellites," Tech. Rep. GKSS 97/E/55, GKSS, 1997.

[16] F. M. Monaldo, D. R. Thompson, R. C. Beal, W. G. Pichel, and P. Clemente-Colón, "Comparison of SAR-derived wind speed with model predictions and buoy comparisons," *IEEE Trans. Geosci. and Remote Sensing*, vol. 39, no. 12, pp. 2587–2600, Dec. 2001.

[17] F. M. Monaldo, D. R. Thompson, W. G. Pichel, and P. Clemente-Colón, "A systematic comparison of QuikSCAT and SAR ocean surface wind speeds," *IEEE Trans. Geosci. and Remote Sensing*, In Press 2003.

[18] J. Horstmann, W. Koch, Winstead N. S, P. Clemente-Colónn F. M. Monaldo, and W. G. Pichel, "Comparison of RADARSAT-1 SAR retrieved ocean wind fields to quikscat and numerical models," in *Proc. International Geoscience and Remote Sensing Symposium*, Toulouse, France, July 2003.

[19] F. M. Monaldo, V. Kerbaol, P. Clemente-Colón, B. Furevik, J. Horstmann, J. Johannessen, X. Li, W. G. Pichel, T. Sikora, D. R. Thompson, and C. C. Wackerman, "The SAR measurement of ocean surface winds," in *Second Workshop on Coastal and Marine Applications of SAR*, Longyearbyen, Spitsbergen, Norway, September 2003.

[20] R. C. Beal, "Toward an international StormWatch using wide-swath SAR," *The Johns Hopkins Univ. Tech. Dig.*, vol. 21, no. 1, pp. 12–20, Jan. 2000.

[21] K. S. Friedman, T. D. Sikora, W. G. Pichel, P. C. Clemente-Colón, and G. Hufford, "Using spaceborne synthetic aperture radar to improve marine surface analyses," *Weather Forecast.*, vol. 16, pp. 270–276, 2001.

[22] W. G. Pichel and P. Clemente-Colón, "NOAA CoastWatch SAR applications and demonstration," *The Johns Hopkins Univ. Tech. Dig.*, vol. 21, no. 1, pp. 49–57, Jan. 2000.

[23] R. B. Stull, *An Intruction to Boundary Layer Meterology*, Kluwer Academic Publishers, 1994.